ACS OMEGA

Open Access

http://pubs.acs.org/journal/acsodf

Article

Tailoring Morphology of MgO with Mg-MOF for the Enhanced Adsorption of Congo Red

Zhuome Duojie, Keru Chen, Jinxin Chen, Qiuming Zeng, Juanjuan Bai, Tingting Li, Cunhua Ma,* and Mingjin Zhang*

Cite This: *ACS Omega* 2024, 9, 41676−41686

Read Online

ACCESS | Metrics & More | Article Recommendations

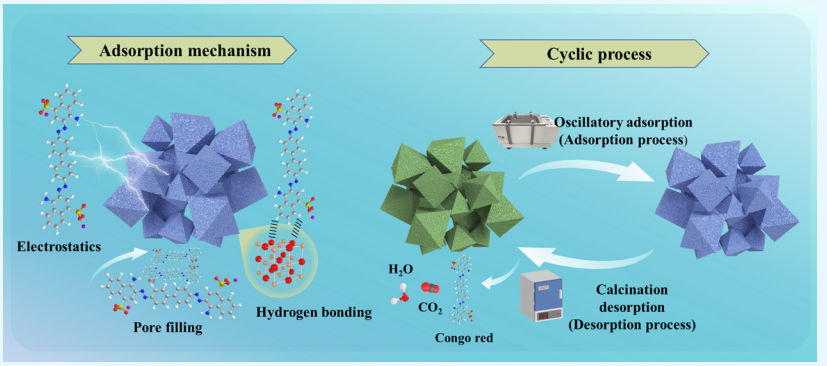

ABSTRACT: The active site is a highly anticipated property of adsorbent in the field of separation, as it enables a concurrent enhancement of both adsorption efficiency and adsorption rate. Herein, employing morphology-oriented regulation, we successfully fabricated heterogeneous MgO adsorbent from a magnesium-based metal−organic framework (MOF) precursor, octahedral MgO-M and laminated sheets MgO-P, for the capture of Congo red (CR). Specifically, the octahedron MgO-M exhibits a greater abundant of moderately and strongly alkaline sites, which facilitate the adsorption of CR. Furthermore, the synergistic effect between alkaline site and lattice oxygen further enhances the adsorption process. The adsorption data align more closely with the Pseudo-second-order kinetic model and Langmuir models. Notably, the exceptional adsorption capacity (exceeding 1900 $mg \cdot g^{-1}$ for MgO-M) and the secondary regeneration efficiency (over 96% removal rate across six cycles) offer promising prospects for future industrial applications, effectively addressing challenges related to poor water stability and difficult storability. Additionally, characterizations reveal the positive roles of alkaline sites, lattice oxygen, and pore structure in capturing significant quantities of CR through mechanisms such as electrostatic interactions, hydrogen bonding, and pore filling.

1. INTRODUCTION

Driven by population growth and economic development, the increase of water pollution resulting from increased human activities and industrialization has exacerbated water scarcity, presenting an increasingly urgent concern in contemporary society.[1−4] Industries frequently utilize organic dyes in their respective processes, which are often discharged improperly into the aquatic environment.[5] These dyes possess complex aromatic structure, as well as physical, chemical, stability and light stability, rendering them nonbiodegradable and causing significant harm to both the environment and human health.[6]

Congo red (CR) is a water-soluble azo-anion dye characterized by a molecular structure comprising six benzene rings.[7] Despite its high toxicity and potential carcinogenic and mutagenic hazards to both aquatic organisms and humans, this compound is extensively used in the textile industry.[8] This toxicity has spurred researchers to develop water purification technologies aimed at promoting the recycling and reuse of water.[9] Among various available water treatment techniques, adsorption treatment is recognized as an optimal method for clarifying wastewater due to its cost-effectiveness, simplicity, efficiency and eco-friendliness.[10,11] While researchers are focusing on innovative studies of adsorbents, each type has inherent drawbacks, including poor stability, low regeneration capacity, and the risk of secondary pollution.[12] Thus, designing high-performance adsorbents poses a significant challenge, particularly for the sustainable remediation of dye-contaminated waters.

Received: June 18, 2024
Revised: September 13, 2024
Accepted: September 18, 2024
Published: September 27, 2024

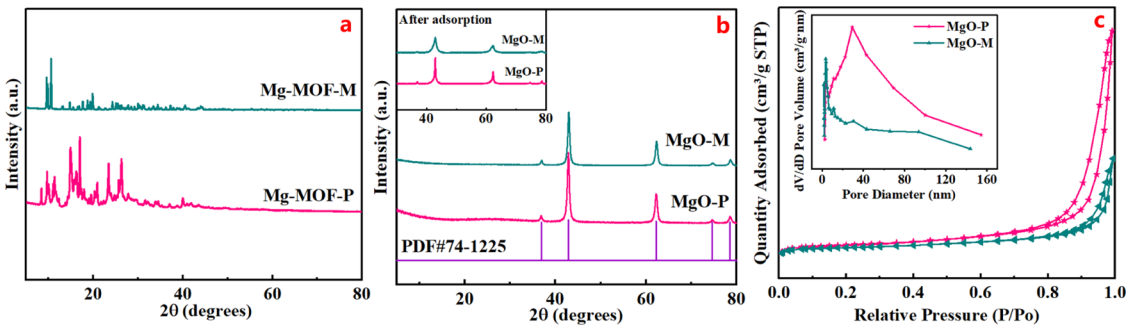

Figure 1. XRD patterns of (a) Mg-MOF, (b) MgO and (c) N_2 adsorption−desorption isotherms of MgO (inset: the corresponding distribution of pore diameter).

MgO is a cost-effective, eco-friendly and readily available adsorbent. Given that water typically contains ions such as Ca^{2+}, Mg^{2+}, MgO is a suitable for treating organic pollutants in water without introducing secondary metal contamination.[13−16] The porosity, surface area, pore size, and morphology of adsorbents, which denote the abundance of active adsorption sites, are critical for effective removal of various organic pollutants from water. In recent years, porous MgO has been widely employed in water treatment.[17,18] For instance, Khan et al. investigated the adsorption mechanism of methyl orange and CR using poly(vinylpyrrolidone)-modified MgO.[19] Li et al. synthesized oxygen-rich defect MgO via the citric acid steam-assisted decomposition method, demonstrating efficient removal capabilities for CR and Ni(II).[20] Xu et al. developed flower-like magnesium oxide and a magnesium oxide-graphene oxide complex through ethylene glycol, achieving a maximum adsorption capacity of reached 237 $mg·g^{-1}$ for CR.[21] Additionally, Li et al. utilized the solvothermal method to produce layered porous MgO materials, attaining a CR adsorption capacity of 666.7 $mg·g^{-1}$.[22]

Metal−organic frameworks (MOFs) and their derivatives have garnered significant attention due to their remarkable properties, including high porosity, extensive specific surface area, accessible active sites, and thermal stability.[6,23−25] By selectively choosing or modifying organic and inorganic components, the structure and porosity of MOFs can be precisely tailored.[26] Compared to traditional metal oxide precursors, MOFs offer a versatile foundation for synthesizing metal oxides, enabling the creation of hierarchical porous structures with enriched active sites and large surface areas. Numerous MOF-derived metal oxides have been reported for their adsorption capabilities regarding Congo red (CR) dyes. For instance, Hu et al. modified a MOF-derived carbon adsorbent, PEI@MDC, with polyethylenimine (PEI), resulting in a significant adsorption capacity of 1700 $mg·g^{-1}$ for CR solutions.[27] Similarly, Wang et al. synthesized MNC HS through a straightforward one-step solvothermal method using ZIF-67 as a precursor, achieving an adsorption capacity of 1194.7 $mg·g^{-1}$ for CR dye.[28] It is important to note that most reported MOFs and their derivatives incorporate transition metals, with modifications enhancing their performance across various applications. However, the design and modification of alkaline earth metal MOFs have received comparatively little attention.

Inspired by the existing literature, this study presents a novel method for synthesizing porous MgO, utilizing Mg-MOF as a precursor through simple air calcination, specifically aimed at capturing CR dyes from wastewater. The favorable adsorption performance and excellent regeneration capabilities underscore the potential of MgO as an effective water purification adsorbent for CR. Additionally, MOF-derived MgO materials exhibit enhanced stability, including water stability and storability, laying a solid foundation for further advancements in the field of alkaline earth metals.

2. RESULTS AND DISCUSSION

2.1. Characterizations of Adsorbent. *2.1.1. Identification of the Prepared Adsorbents.* The physical structural properties of all adsorbents were initially examined through X-ray diffraction (XRD), nitrogen (N_2) adsorption−desorption analysis, and scanning electron microscopy (SEM). XRD patterns were utilized to assess the crystal structures of the prepared samples. The XRD patterns of the two Mg-MOF samples (Figure 1a) were found to be in complete agreement with those reported in the literature,[1,26,29] while both MgO samples exhibited all characteristic peaks associated with MgO (PDF#74−1225) as shown in Figure 1b. This finding confirms that the Mg-MOF precursors were successfully converted into MgO samples following calcination, irrespective of the ligands used, thereby demonstrating that MgO materials were effectively synthesized using MOFs as precursors. Additionally, the sharp diffraction peaks observed for both Mg-MOF and MgO indicate that the samples possess good crystallinity. As illustrated in the inset of Figure 1b, all peaks of the MgO materials postadsorption remained intact, further confirming the stability of the synthesized MgO materials.

Figure 1c presents the N_2 adsorption−desorption curves along with the pore size distributions for the two MgO samples. Both MgO adsorbents exhibited type IV adsorption isotherms accompanied by H3 hysteresis loops,[30] indicating a porous structure characterized by typical slit-shaped pores,[31] which arise from the closely packed thin sheets of MgO-P and the surface defects of MgO-M. The pore size distribution curve (Figure 1c, inset) distinctly reveals that the primary pore size for MgO-M is concentrated within the 2−20 nm mesoporous range, while MgO-P displays a distribution of 2−50 nm mesopores and 50−100 nm macropores. This observation further suggests that the rich pore structure of MgO is a result of the Mg-MOF. The favorable aperture-to-particle size ratio of MgO-M in relation to the CR molecule (0.9−2 nm) facilitates the effective ingress of CR dye, significantly reducing the transport path for dye molecules and thereby enhancing the adsorption kinetics of the adsorbents.[32,33] Subsequent adsorption experiments corroborated these findings.

https://doi.org/10.1021/acsomega.4c05680
ACS Omega 2024, 9, 41676−41686

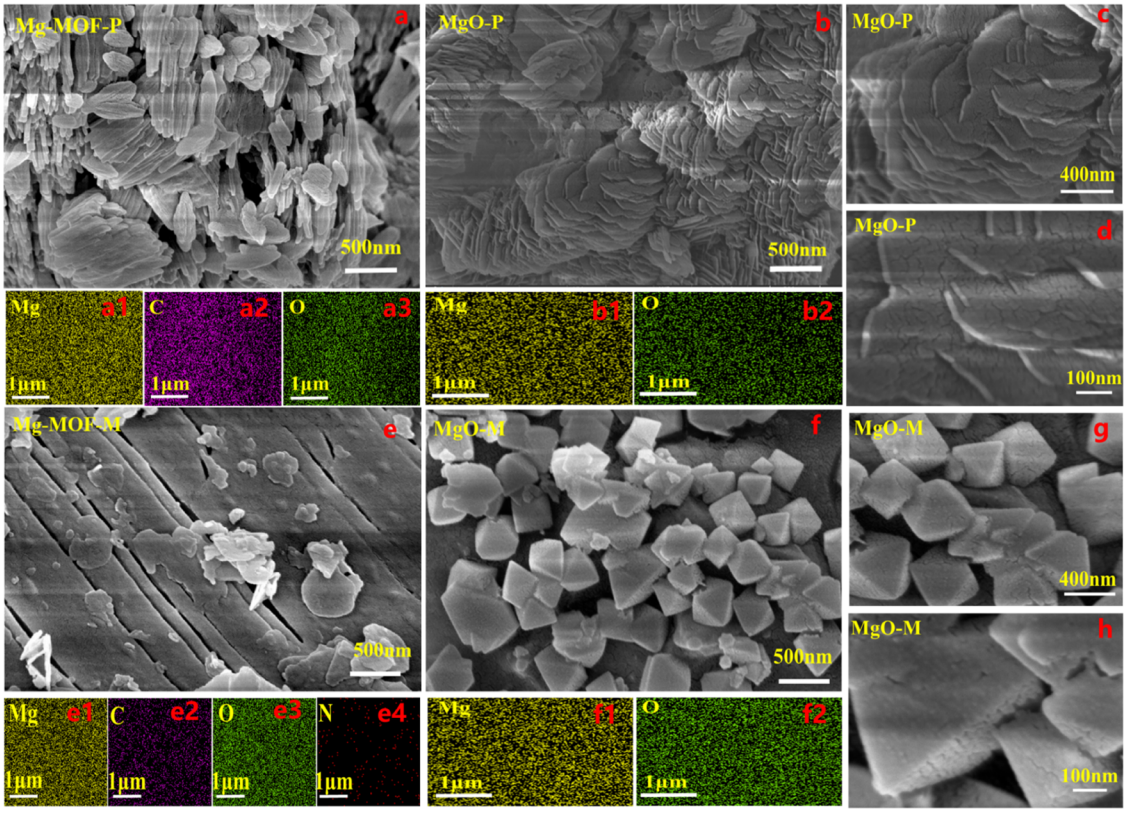

Figure 2. SEM images of (a) Mg-MOF-P, (b, c, d) MgO-P, (e) Mg-MOF-M and (f, g, h) MgO-M, and EDX mapping of (a1−a3) Mg-MOF-P, (b1, b2) MgO-P, (e1−e4) Mg-MOF-M and (f1, f2) MgO-M.

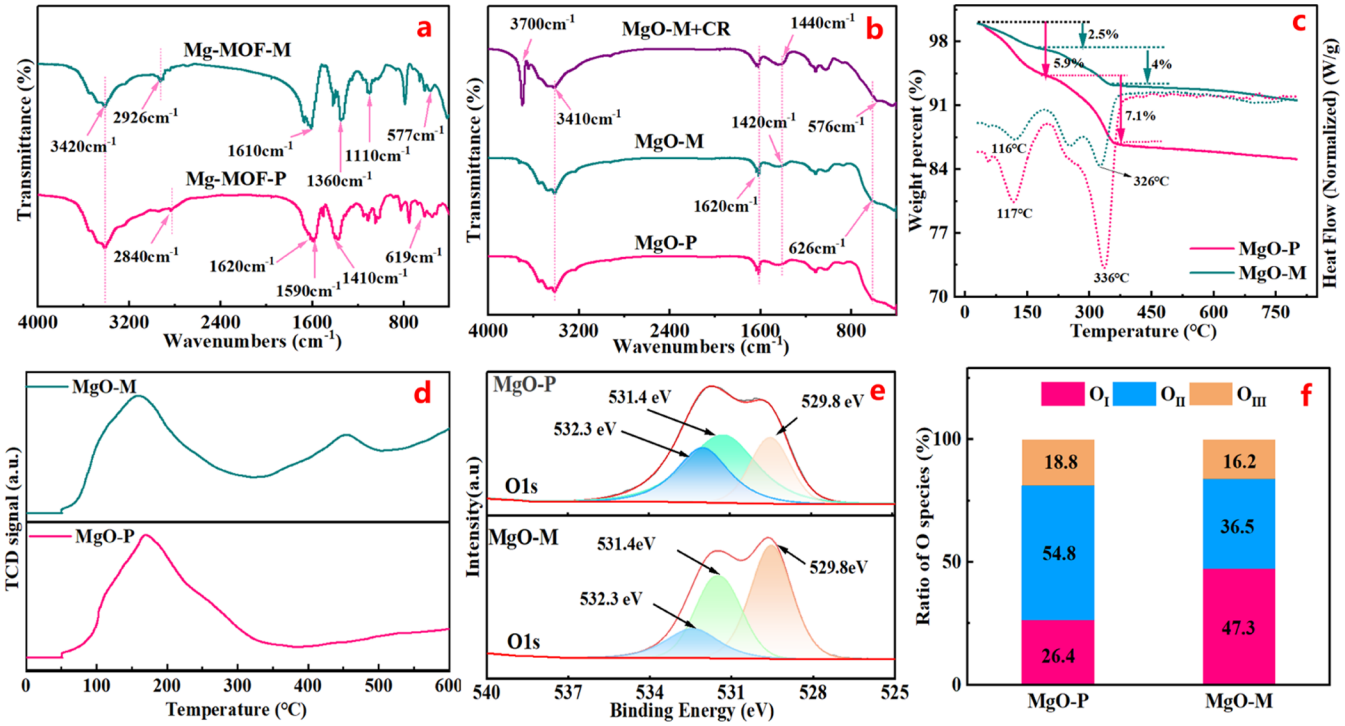

Figure 3. FTIR spectra of (a) Mg-MOF and (b) MgO. (c) TGA diagrams, (d) CO_2-TPD tests and (e, f) XPS survey spectra of MgO.

The surface morphologies of the Mg-MOF and MgO samples were further analyzed using scanning electron microscopy (SEM). Figure 2a illustrates that the Mg-MOF-P precursor exhibits an irregular nanosheet appearance. Following calcination in an air atmosphere, the resulting product, MgO-P (Figure 2b,2c), retains a similar shape but displays laminated sheets. This outcome suggests that the nanosheet structure of the Mg-MOF-P precursor was well preserved. The

https://doi.org/10.1021/acsomega.4c05680
ACS Omega 2024, 9, 41676−41686

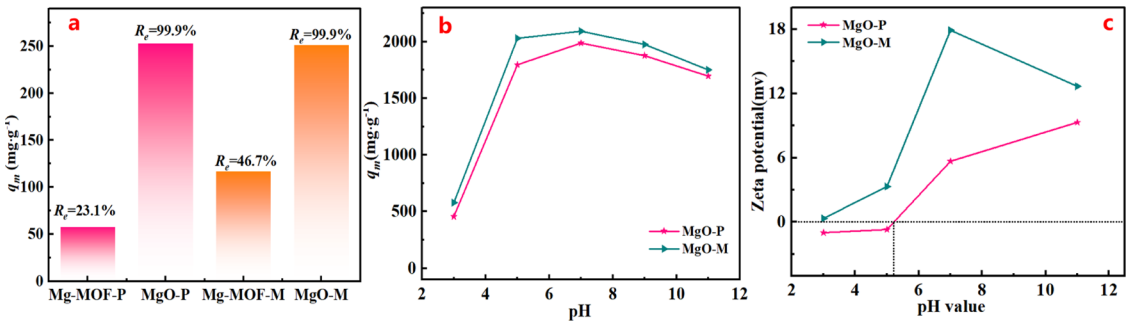

Figure 4. (a) The adsorption capacity and removal rate of Mg-MOF and MgO materials on Congo red dyes (298k), (b) the effect of initial solution pH and (c) ζ-potential of MgO materials.

proposed structural evolution process aligns with our expected strategy. Additionally, the Mg-MOF-M precursor exhibits a layered structure morphology, with some nanoparticles forming on the surface (Figure 2e). The MgO-M particles, which are the products obtained after the calcination of Mg-MOF-M in an air atmosphere, show a uniformly regular octahedral shape (Figure 2f,2g). A notable morphological characteristic of the MgO samples is the presence of abundant defect structures on their surfaces (Figure 2d,h), these defects are promising candidates for adsorption sites.[34,35] Elemental mapping images (Figure 2a1−a3,2e1−e4) indicate the presence of Mg, O, and C in Mg-MOF-P, and Mg, O, C, and N in Mg-MOF-M. However, the N signals in Mg-MOF-M are sparse, suggesting a low mass fraction of nitrogen in the materials based on the Methylimidazole ligand. No nitrogen or carbon was detected in the MgO samples (Figure 2b1,b2,f1,f2), confirming that only magnesium and oxygen were present as the characteristic elements in the two MgO materials, thus validating that the MgO samples derived from Mg-MOFs were successfully prepared.

2.1.2. Chemical Properties of MgO Adsorbents. The chemical properties of all samples were investigated using Fourier-transform infrared (FTIR) spectroscopy, thermogravimetric analysis (TGA), CO_2-temperature-programmed desorption (CO_2-TPD), and X-ray photoelectron spectroscopy (XPS). In the FTIR spectra of the two Mg-MOFs (Figure 3a), significant peaks at 3420 and 1620 cm^{-1} are attributed to −OH stretching.[36] For Mg-MOF-P, the asymmetric vibration of the C−H bond occurs at 2840 cm^{-1}, while the vibration peak of the C═C bond is observed at 1590 cm^{-1}[37,38] The characteristic peaks at 1410 and 619 cm^{-1} correspond to the Mg−O−Mg and Mg−O bonds, respectively.[39] In contrast, for Mg-MOF-M, the characteristic absorption peak at 2926 cm^{-1} corresponds to the stretching vibration of the C−H bond in the imidazole ring. The absorption peaks at 1610 and 1360 cm^{-1} are attributed to the bending vibrations of the C═N and C−N bonds in 2-methylimidazole, respectively, while the bending vibration of the $-CH_3$ group in 2-methylimidazole is noted at 1510 cm^{-1}.[7,40,41] The characteristic peak at 1110 cm^{-1} corresponds to the in-plane bending vibration of the imidazole ring, and the peak at 577 cm^{-1} is attributed to the tensile vibration of the Mg−N bond.

In the FTIR spectrum of the MgO-P and MgO-M materials (Figure 3b), the characteristic peaks at 3410 and 1620 cm^{-1} correspond to the absorption of hydrate −OH on the surface of the materials,[42] while the characteristic deformation vibration peak at 1420 cm^{-1} corresponds to Mg−O−Mg. The absorption peak at 626 cm^{-1} is characteristic of the Mg−O bond. A comparison of the FTIR spectra reveals a prominent vibration peak at 3700 cm^{-1} for −OH after CR adsorption, which was absent prior to CR adsorption. This suggests that the MOFs-derived template MgO materials exhibit good stability in air, addressing the instability of traditional MgO materials under atmospheric conditions.[39]

Most precursors of Mg-MOF generate volatile gases during calcination, leaving a small quantity of residual carbon in the materials. Since the presence of carbon can negatively impact the adsorption performance of the adsorbent, thermogravimetric analysis (TGA) was utilized to quantify the specific carbon content in the two MgO samples (Figure 3c). The TGA curves indicate a three-stage pyrolysis process. The initial weight loss occurring below 250 °C is attributed to the evaporation of water and some organic volatiles adsorbed on the MgO surface, whereas the weight loss observed between 250−375 °C is due to the loss of residual carbon. A comparison of the weight loss curves reveals that the carbon content in MgO-P and MgO-M is 7.1 and 4%, respectively. The lower residual carbon content in MgO-M is advantageous for the adsorption of Congo Red (CR) compared to MgO-P. Notably, the thermal stability of both MgO materials can reach 730 K in an air atmosphere, which is attributed to their high electro positivity, leading to strong ionic-like bonds with carboxylate-based or imidazole-based organic ligands.

MgO adsorbents typically contain various types of adsorption active sites, each playing a distinct role in the dye adsorption process. To identify the dye adsorption sites in different MgO adsorbents, CO_2 temperature-programmed desorption (TPD) tests were conducted to analyze the surface alkaline active sites. In the CO_2-TPD spectrum (Figure 3d), a higher peak temperature and peak area indicate a greater number of alkaline centers, suggesting an increased presence of alkaline active sites. The temperature ranges of 100−300, 300−550 °C, and above 550 °C correspond to weak, medium, and strong basic active sites, respectively. The Fourier-transform infrared (FT-IR) spectrum (Figure 3b) shows that the MgO surface sequentially presents −OH, O^{2-}, and Mg^{2+} groups, which correlate with enhanced basicity and correspond to weak, medium, and strong basic sites, respectively. In contrast, the CO_2-TPD spectra indicate that the MgO-M adsorbent contains weak, medium, and strong basic sites, while MgO-P is characterized as a weakly basic adsorbent with only weak basic sites. In conclusion, the presence of more basic active sites significantly enhances the adsorption of CR. This finding aligns with the observed adsorption performance of the two materials concerning CR dye, where the adsorption capacity was greater for MgO-M compared to MgO-P.

https://doi.org/10.1021/acsomega.4c05680
ACS Omega 2024, 9, 41676−41686

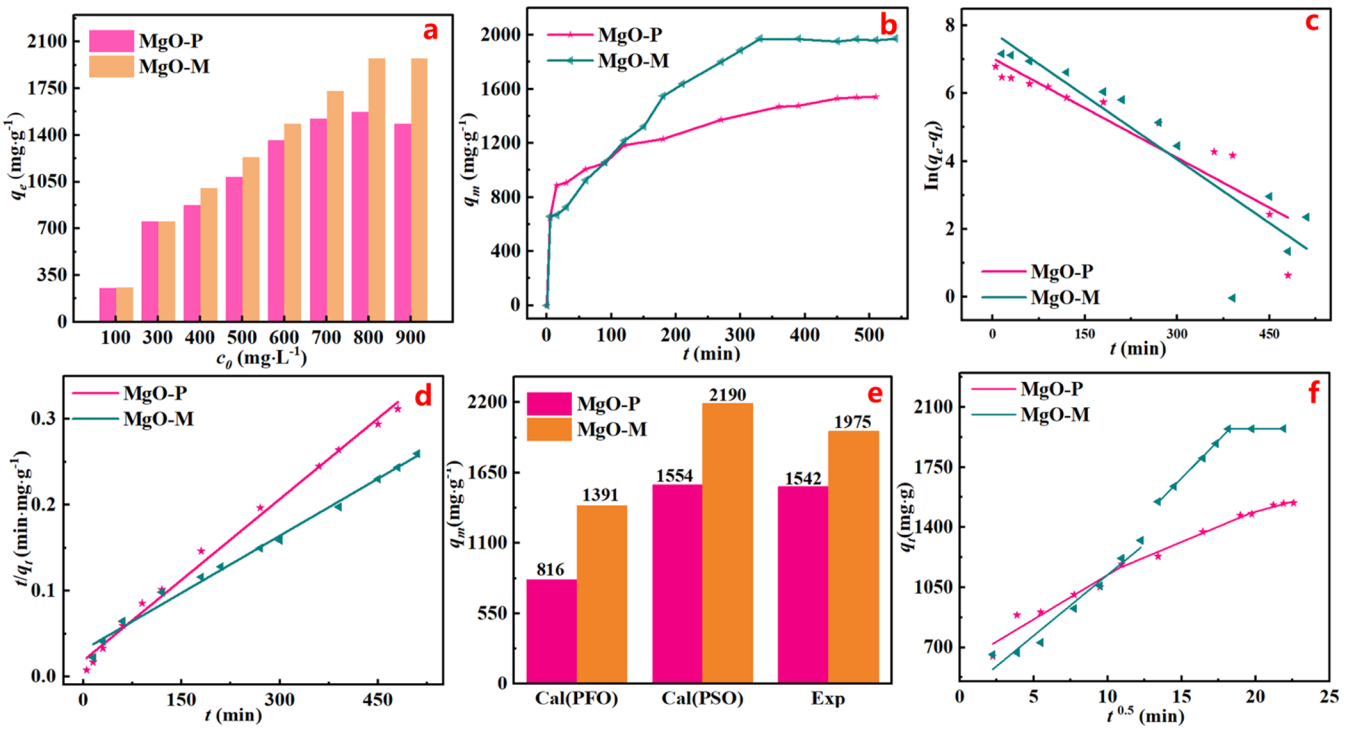

Figure 5. Evolution of CR adsorption capacity of MgO materials over (a) initial concentration and (b) time (298 K, V = 300 mL, c_0 = 800 mg·L^{-1}), (c) PFO kinetic model, (d) PSO kinetic model, (e) $q_{e,\ exp}$ and $q_{e,cal}$ and (f) intraparticle diffusion model at 298 K for CR dye adsorption by MgO materials.

X-ray photoelectron spectroscopy (XPS) was employed to analyze the electronic structure of the surfaces of the MgO materials. Figure 3e presents high-resolution XPS spectra for the primary element, O 1s. The O 1s spectra (Figure 3e) of both MgO samples exhibited three peaks, corresponding to lattice oxygen (O_I), oxygen vacancies (O_{II}), and adsorbed oxygen (O_{III}), with peak positions at 529.8, 531.4, and 532.3 eV, respectively.[43−45] In Figure 3f, the content of lattice oxygen (O_I) in MgO-M was calculated to be 47.3%, significantly exceeding that of MgO-P, which was 26.4%. Subsequent results indicate that MgO-M outperforms MgO-P in terms of adsorption capacity. Thus, it can be concluded that lattice oxygen surrounding Mg serves as the primary active absorption centers in MgO material.[46]

2.2. MgO Adsorption Performance. To evaluate the adsorption performance of Mg-MOF material on CR, this study utilized a specific concentration of CR solution as the initial sample and examined the adsorption behavior of CR with Mg-MOF at 25 °C. The results, illustrated Figure 4a, show that the adsorption capacities of Mg-MOF-P and Mg-MOF-M for Congo Red were only 57.85 and 116.71 mg·g^{-1}, respectively, with corresponding removal rates of merely 23.1 and 46.6%. However, following the calcination of the Mg-MOF material, the adsorption capacities increased to 253.1 and 251.52 mg·g^{-1}, with removal rates approaching 99.99%. This enhancement is well-documented in the literature and can be attributed to the calcination process, which introduces more defects in the MgO material.[47] Consequently, the calcined MgO material exhibits an increased number of active sites, thereby improving its adsorption performance for CR.[48−50] Furthermore, this performance will be substantiated by subsequent characterization and performance assessments.

The pH value of a solution is a significant factor influencing the adsorption of dye molecules. The adsorption of Congo Red (CR) dyes was examined across a pH range of 3−11, with results depicted in Figure 4b. For the MgO-P and MgO-M materials, the adsorption capacity of CR increased from 450.01 to 1987.66 mg·g^{-1} and from 579.43 to 2092.09 mg·g^{-1}, respectively, as the pH of the CR solution rose from 3 to 7. This phenomenon can be attributed to the surface charges of the adsorbent and dye molecules at varying pH levels. In the lower pH range, the surface of the hydrated oxide (MOH) is predominantly covered by H^+ ions. Consequently, as the pH of the CR solution increases from 3 to 7, the electrostatic attraction between the positively charged MgO materials and the negatively charged CR dye molecules enhances the adsorption of the dye. However, as the pH of the CR solution rises from 7 to 11, the adsorption capacity of CR gradually decreases. In this higher pH range, MOH may react with hydroxide ions to form a negatively charged deprotonated oxide (MO^-). Therefore, at pH values greater than 7, the formation of MO^- on the surface of the MgO material competes with the negatively charged CR dye molecules for active sites.[6,39] This indicates that the optimal adsorption pH for the CR solution is 7.

The potential change on the material surface was investigated by characterizing the ζ-potential of the adsorbent at different pH conditions, and the results are shown in Figure 4c. The isoelectric point (IEP) of MgO-P is 5.15, indicating that the MgO material surface is negatively charged at pH less than 5.15 and positively charged at pH more than 5.15. Moreover, the ζ-potential of MgO-M material indicates a positive within the pH range of 3−11, indicating that the material surface is positively charged in this range. As an anionic substance, CR can be adsorbed onto samples through electrostatic interaction. The $-SO^{3-}$ group in the CR molecule is attracted to the positively charged surface of the MgO material, thereby achieving the removal effect. This conclusion

https://doi.org/10.1021/acsomega.4c05680
ACS Omega 2024, 9, 41676−41686

Table 1. PFO Model and PSO Model Parameters for CR Adsorption on MgO Materials

		PFO model			PSO model		
samples	$q_{e,\ exp}$ (mg·g^{-1})	$q_{e,\ cal1}$ (mg·g^{-1})	k_1 (min^{-1})	R^2	$q_{e,\ cal2}$ (mg·g^{-1})	k_2 (g·mg^{-1}·min^{-1})	R^2
MgO-P	1542.03	815.662	0.0111	0.843	1554.726	1.79×10^{-5}	0.993
MgO-M	1975.19	1391.309	0.0144	0.798	2190.101	5.92×10^{-6}	0.990

Table 2. Intra-particle Diffusion Model Parameters for CR Adsorption by MgO Materials

	intraparticle diffusion								
samples	k_{dif1} (mg·min$^{-1/2}$·g^{-1})	C_1	R^2	k_{dif2} (mg·min$^{-1/2}$·g^{-1})	C_2	R^2	k_{dif3} (mg·min$^{-1/2}$·g^{-1})	C_3	R^2
MgO-P	59.8	663.8	0.890	38.7	819.3	0.977	29.5	1138.1	0.824
MgO-M	77.4	468.1	0.951	90.6	387.6	0.998	0.56	1965.0	0.981

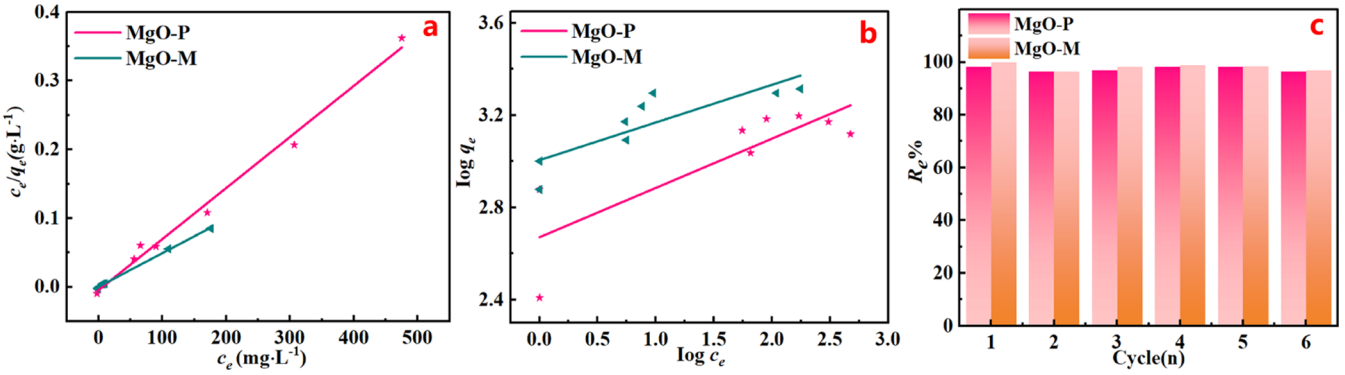

Figure 6. (a) Langmuir isotherm and (b) Freundlich isotherm at 298 K for CR dye adsorption by MgO materials, (c) the regeneration experiments at 298 K of MgO materials.

is consistent with the pH value and further validates the reaction mechanism.

Figure 5a illustrates the effect of the initial concentration (c_0) of CR on the adsorption capacity. As c_0 increases, the adsorption capacity (q_t) of both materials for CR also rises. However, beyond a certain concentration, q_t begins to decline, likely due to the saturation of active sites on the material's surface by CR molecules. Additionally, the relationship between q_t and adsorption time (t) for CR adsorption on MgO materials was examined at a concentration of CR c_0 = 800 mg·L^{-1}. The $q_t \sim t$ curve (Figure 5b) shows an initial upward trend within the first few minutes. As time progresses, the adsorption rate of both MgO adsorbents for CR gradually decreases, ultimately leading to a flattening of the curve. Notably, the q_t of MgO-M surpasses that of MgO-P, with MgO-M exhibiting an adsorption capacity of 1975 mg·g^{-1} at 330 min, while MgO-P shows a capacity of 1542 mg·g^{-1} at 450 min, indicating adsorption equilibrium.

Furthermore, pseudo-first-order (PFO), pseudo-second-order (PSO), and intraparticle diffusion models were employed to analyze the adsorption data of MgO.[51] The fitted curves and kinetic model parameters are presented in Figure 5c,d and Table 1, respectively. It is evident that the best matching coefficient R^2 of the PSO linear graph is closer to 1 (0.993 and 0.990) compared to that of the PFO linear graph (0.843 and 0.798). Moreover, the theoretical calculated values of equilibrium adsorption ($q_{e,cal}$) from the PSO model closely align with the actual experimental data ($q_{e,exp}$) (Figure 5e and Table 1). These findings indicate that the adsorption of CR dyes by the two MgO materials is more consistent with the PSO kinetic model, suggesting that chemisorption is the rate-determining step in the adsorption of CR.[52]

Based on the fitting linear diagram and the associated data from the intraparticle diffusion model (Figure 5f and Table 2), the diffusion process of CR across the two MgO materials can be categorized into three distinct stages. These stages correspond to rapid CR diffusion from the solution to the adsorbent, transportation within the internal pores, and the final adsorption equilibrium.[53,54] The three-stage linear plots illustrate a segmented yet continuous adsorption process, with the kinetic constant (slope k) serving as an indicator of the adsorption rate.[55]

For MgO-P, the relationship $k_{dif1} > k_{dif2} > k_{dif3}$ suggests that CR diffusion from the solution to the adsorbent occurs rapidly, while the transport within the internal pores is comparatively slower. This indicates that the 2−50 nm mesopores and 50−100 nm macropores of MgO-P, along with its weaker basic adsorption sites, are less favorable for CR adsorption. In contrast, for MgO-M, the relationship $k_{dif2} > k_{dif1} > k_{dif3}$ indicates that CR diffusion from the solution to the adsorbent is rapid, and the transportation within the internal pores is even faster. This suggests that the 2−20 nm mesopores of MgO-M and its stronger basic adsorption sites significantly enhance CR adsorption. Furthermore, in the initial two stages of diffusion, the values of kdif1 and kdif2 for the MgO-M system are approximately 1.4 and 2.4 times greater than those of the MgO-P system, highlighting a more vigorous and rapid diffusion process. Considering the aperture data, the favorable aperture-to-particle size ratio of MgO-M relative to the CR molecule facilitates more effective and rapid diffusion of CR, significantly reducing the transport path for dye molecules and thereby enhancing the adsorption kinetics of the adsorbents. Consequently, MgO-M demonstrates superior CR adsorption capacity.

https://doi.org/10.1021/acsomega.4c05680
ACS Omega 2024, 9, 41676−41686

Table 3. Adsorption Isotherms Parameters for CR Adsorption by MgO Materials

	Langmuir isotherm model				Freundlich isotherm model		
samples	q_{max} (mg·g^{-1})	K_L	R^2	R_L	K_f (mg·g^{-1})	$1/n$	R^2
MgO-P	1400	1.556	0.989	0.000743	600	0.271	0.653
MgO-M	2015	1.8	0.998	0.000694	1138	0.205	0.671

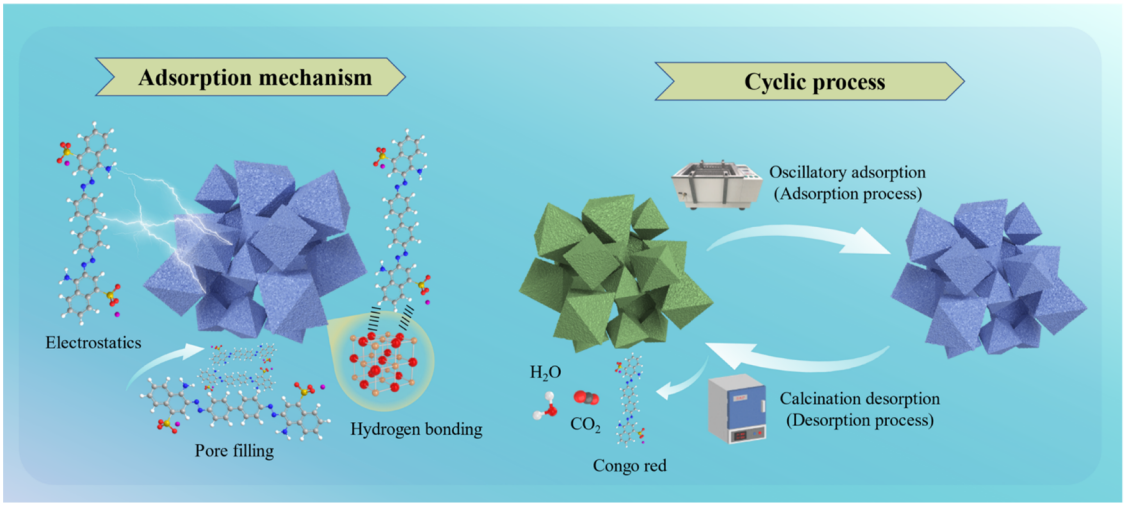

Figure 7. Adsorption mechanism process and cyclic process of MgO materials.

To enhance our understanding of the adsorption mechanism, we analyzed the adsorption isotherms of Congo Red (CR) on two MgO materials. The analysis revealed a strong fit to the Langmuir model, with an R^2 value exceeding 0.98 (Figure 6a), indicating that the adsorption of CR on MgO occurs as a monolayer. Notably, the theoretical maximum adsorption capacities (q_{max}) derived from the Langmuir model for the two MgO materials were calculated to be 1400 and 2015, respectively, which closely aligned with the experimental values. Additionally, the equilibrium factor (R_L) derived from the Langmuir isothermal equation ranged from 0.00448 to 0.00694 (Table 3), suggesting that the adsorption of CR on the MgO materials is favorable.[56,57]

2.3. Recyclability and Stability. To further assess the superior recovery and stability of MgO, we measured the recyclability of the adsorbent, with the cycle progression illustrated in Figure 7. Both MgO samples maintained their adsorption performance above a 96% removal rate after six cycles, demonstrating excellent reusability. The slight decrease in removal rate may be attributed to minor adsorbent loss.[58] Furthermore, the XRD (Figure 1b, inset), FT-IR (Figure 3b inset), XPS (Figure 8a) and energy dispersive X-ray spectroscopy (EDS) elemental (Figure 8b) of the MgO materials post-CR adsorption exhibited no significant changes, indicating that the adsorption process did not alter the structure of MgO. These findings confirm that MOF-derived MgO possesses superior adsorption activity and structural stability.[59]

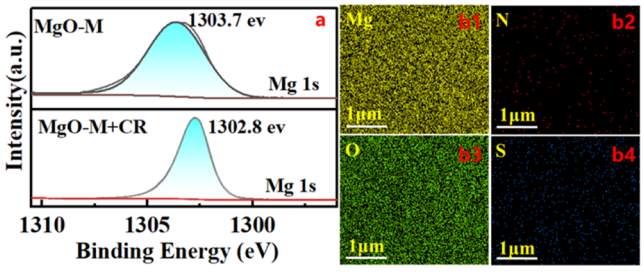

Figure 8. (a) XPS and (b1−4) EDS diagram of MgO-M after CR adsorption.

2.4. CR Adsorption Mechanism. The adsorption mechanism of the MgO adsorbent is illustrated in Figure 7. Currently, the primary mechanisms by which MgO interacts with CR are believed to involve hydrogen bonding, electrostatic interactions, and hole-filling,[60−63] as supported by XPS, FT-IR, and Brunauer−Emmett−Teller (BET) analysis. Figure 8b, presents the EDS elemental mapping results, which confirm the presence of nitrogen (N) and sulfur (S) in the postadsorption MgO-M adsorbent, indicating successful adsorption of CR, which contains both N and S atoms, onto the MgO-M surface. Furthermore, a comparison of the functional groups in MgO-M after adsorption with those in raw MgO (Figure 3b) reveals a broad absorption band at 1440 cm^{-1}, attributable to the C═C stretching vibration of the benzene ring in the CR molecules. Additionally, an adsorption peak at 576 cm^{-1} corresponds to the stretching vibration of the S−O bond in the adsorbed CR molecules. The observed shift of the peak from 626 to 576 cm^{-1} due to CR adsorption further supports this conclusion, suggesting that CR was effectively adsorbed onto the MgO materials.

The adsorption of CR dye onto MgO is primarily driven by electrostatic attraction. As illustrated in Figure 8a, there are notable changes in the peak intensities and elemental composition of magnesium (Mg) upon the adsorption of CR onto the surface of MgO-M. Specifically, the intensity of the characteristic Mg peak decreases, and the binding energy of this peak shifts from 1303.7 to 1302.8 eV, which indicates a strong electrostatic interaction between MgO-M and CR.[64] This reduction in binding energy is likely attributed to an increase in electron density on the electron-deficient Mg, facilitated by the electron-rich nature of CR. Furthermore, as shown in Figure 4b,4c the isoelectric point (IEP) of MgO is

https://doi.org/10.1021/acsomega.4c05680
ACS Omega 2024, 9, 41676−41686

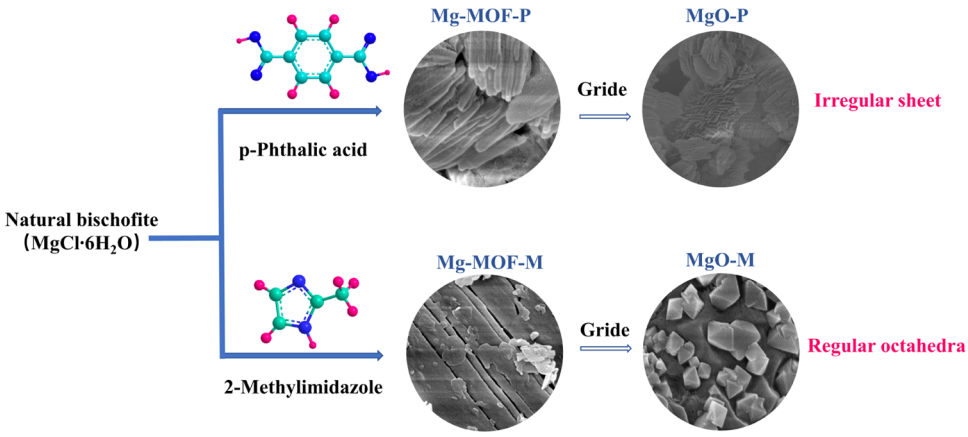

Figure 9. Preparation process of Mg-MOF and MgO.

approximately 5.15. When the pH of the CR solution exceeds the IEP, CR molecules can be effectively removed through strong electrostatic attraction.[17,65,66]

Additionally, the Mg-MOF derived MgO exhibits a low content of functional groups, such as hydroxyl (−OH) groups. The adsorption of CR dye from aqueous solutions occurs via hydrogen bonding between these hydroxyl groups, which act as hydrogen acceptors, and the sulfonic acid groups of CR, which serve as hydrogen donors (Figure 7). Lastly, CR is also adsorbed from aqueous solutions through hole filling, facilitated by the suitable pore sizes and the porous structure of MgO.

3. CONCLUSIONS

A regular octahedral MgO-M with rich mesoporous (2−20 nm) and an irregular laminated MgO-P with extensive mesoporous (2−50 nm) and mesoporous (50−100 nm) were synthesized for the first time using a simple solvothermal method with a metal−organic framework (MOF) as precursor. These materials were employed as adsorbents for the capture of Congo Red (CR) dye from water. Comprehensive characterization revealed that the octahedral MgO-M, possessing an optimal aperture-to-particle size ratio, exhibited superior dispersibility, leading to the presence of abundant strong basic sites and surface lattice oxygen. Consequently, MgO-M demonstrated a significantly enhanced ability to activate CR (q_e = 1975 mg·g^{-1}). Both MgO materials retained the skeletal structure of the Mg-MOF, which contributed to their excellent water stability and storability, with a CR dye removal rate consistently exceeding 96% over six cycles. This study offers valuable insights for the design of MgO with varied morphologies, pore diameters, and enhanced stability.

4. MATERIALS AND METHODS

4.1. Materials. CR dye ($C_{32}H_{22}N_6Na_2O_6S_2$), *N*,*N*-dimethylformamide (DMF), 2-methylimidazole and *p*-phthalic acid were obtained from macklin.cn. All chemicals and reagents were used as received without further purification. Natural bischofite ($MgCl_2·6H_2O$, ≥96 wt %) was sourced from Qarhan Salt Lake in Qinghai Province and was also utilized without additional purification, Deionized water was employed to prepare all working solutions.

4.2. Synthesis of Mg-MOF Precursor. The Mg-MOF precursor was synthesized using a standard solvothermal method that involved organic ligands, specifically *p*-phthalic acid and 2-methylimidazole, along with natural bischofite and DMF as starting materials. Initially, 1 mmol of *p*-phthalic acid was completely dissolved in 20 mL of DMF under magnetic stirring at 25 °C. Stirring was continued until the mixture formed a homogeneous solution, referred to as solution A. In a separate procedure, 1 mmol of natural bischofite was added to another 20 mL of DMF and stirred magnetically until it completely dissolved, resulting in a homogeneous solution designated as solution B. While maintaining stirring, solution A was gradually added to solution B. The resultant mixture was then transferred to an autoclave and maintained at 125 °C for 24 h. Following this, the autoclave was allowed to cool naturally to room temperature (RT). The resulting suspension was subjected to centrifugation, washed several times with methanol and DMF, and the resulting white powder was dried at 60 °C for 12 h to obtain Mg-MOF-P.

Likewise, the same procedure was replicated to synthesize Mg-MOF-M using 2-methylimidazole as the organic ligand.

4.3. Synthesis of MgO. Mg-MOF-P was ground using an agate mortar for 1 min and subsequently calcined at 550 °C in a muffle furnace for 3 h, resulting in the formation of MgO-P nanoparticles powder. Similarly, by repeating the aforementioned synthesis steps, MgO-M was prepared from Mg-MOF-M. The preparation process for both Mg-MOF and MgO is illustrated in Figure 9.

4.4. Characterization Techniques. The structural characteristics of Mg-MOF and MgO materials, both prior to and following adsorption, were analyzed using a variety of techniques, including X-ray diffraction (XRD), scanning electron microscopy (SEM), Fourier-transform infrared spectroscopy (FTIR), thermogravimetric analysis (TGA), X-ray photoelectron spectroscopy (XPS), CO2 programmed thermal desorption (CO2-TPD), Brunauer−Emmett−Teller (BET) analysis, energy dispersive X-ray spectroscopy (EDS), and ζ-potential measurements.

4.5. Adsorption Experiments. The batch experiments were conducted to investigate the adsorption performance of two MgO adsorbents on CR dye in wastewater. The study examined the effects of contact time and initial concentration of CR to analyze the adsorption kinetics and isotherms. A predetermined optimal amount of adsorbent was added to a fixed volume and concentration of the CR solution. The mixture was then continuously shaken at room temperature (25 °C) for 4 h in a constant temperature shaker to ensure the establishment of adsorption equilibrium and the formation of uniformly dispersed suspensions. Subsequently, approximately

https://doi.org/10.1021/acsomega.4c05680
ACS Omega 2024, 9, 41676−41686

4 mL of the suspension was collected at predetermined time intervals, centrifuged, and the supernatant liquid was analyzed. The amounts of CR adsorption (q_e and q_t, mg·g^{-1}) and the removal rate (R_e %) were determined using eqs 1, 2 and 3

$$q_e = (c_0 - c_e) \times \frac{V}{m} \quad (1)$$

$$q_t = (c_0 - c_t) \times \frac{V}{m} \quad (2)$$

$$R_e\% = \frac{(c_0 - c_e)}{c_0} \times 100 \quad (3)$$

where, c_0 (mg·L^{-1}) is the initial concentration of CR solution, c_e (mg·L^{-1}) is equilibrium concentration at adsorption equilibrium. Additionally, V (L) is the volume of CR solution, and m (g) indicates the mass of MgO adsorbent.

AUTHOR INFORMATION

Corresponding Authors

Cunhua Ma − *School of Chemistry and Chemical Engineering/Qinghai Provincial Key Laboratory of Advanced Technology and Application of Environmental Functional Materials, Qinghai Normal University, Xining 810008, China*; orcid.org/0000-0001-6250-443X; Email: 20211001@qhnu.edu.cn

Mingjin Zhang − *School of Chemistry and Chemical Engineering/Qinghai Provincial Key Laboratory of Advanced Technology and Application of Environmental Functional Materials, Qinghai Normal University, Xining 810008, China*; Email: zhangmingjin@qhnu.edu.cn

Authors

Zhuome Duojie − *School of Chemistry and Chemical Engineering/Qinghai Provincial Key Laboratory of Advanced Technology and Application of Environmental Functional Materials, Qinghai Normal University, Xining 810008, China*

Keru Chen − *School of Chemistry and Chemical Engineering/Qinghai Provincial Key Laboratory of Advanced Technology and Application of Environmental Functional Materials, Qinghai Normal University, Xining 810008, China*

Jinxin Chen − *School of Chemistry and Chemical Engineering/Qinghai Provincial Key Laboratory of Advanced Technology and Application of Environmental Functional Materials, Qinghai Normal University, Xining 810008, China*

Qiuming Zeng − *School of Chemistry and Chemical Engineering/Qinghai Provincial Key Laboratory of Advanced Technology and Application of Environmental Functional Materials, Qinghai Normal University, Xining 810008, China*

Juanjuan Bai − *School of Chemistry and Chemical Engineering/Qinghai Provincial Key Laboratory of Advanced Technology and Application of Environmental Functional Materials, Qinghai Normal University, Xining 810008, China*

Tingting Li − *School of Chemistry and Chemical Engineering/Qinghai Provincial Key Laboratory of Advanced Technology and Application of Environmental Functional Materials, Qinghai Normal University, Xining 810008, China*

Complete contact information is available at: https://pubs.acs.org/10.1021/acsomega.4c05680

Notes

The authors declare no competing financial interest.

ACKNOWLEDGMENTS

This work was financially supported by the Young and Middle-Aged Research Foundation of Qinghai Normal University (2023QZR020).

REFERENCES

(1) Jin, Y.; Liu, F.; Li, Y.; Du, Q.; Song, F.; Chen, B.; Chen, K.; Zhang, Y.; Wang, M.; Sun, Y.; Zhao, S.; Jing, Z.; Pi, X.; Wang, Y.; Wang, D. Efficient adsorption of azo anionic dye Congo Red by micro-nano metal-organic framework MIL-68(Fe) and MIL-68(Fe)/chitosan composite sponge: Preparation, characterization and adsorption performance. *Int. J. Biol. Macromol.* **2023**, *252*, No. 126198.

(2) Ahmed, M. A.; Mohamed, A. A. The use of chitosan-based composites for environmental remediation: A review. *Int. J. Biol. Macromol.* **2023**, *242* (2), No. 124787.

(3) Mussa, Z. H.; Al-Ameer, L. R.; Al-Qaim, F. F.; Deyab, I. F.; Kamyab, H.; Chelliapan, S. A comprehensive review on adsorption of methylene blue dye using leaf waste as a bio-sorbent: isotherm adsorption, kinetics, and thermodynamics studies. *Environ. Monit. Assess.* **2023**, *195* (8), No. 940.

(4) Fuller, R.; Landrigan, P. J.; Balakrishnan, K.; Bathan, G.; Bose-O'Reilly, S.; Brauer, M.; Caravanos, J.; Chiles, T.; Cohen, A.; Corra, L.; Cropper, M.; Ferraro, G.; Hanna, J.; Hanrahan, D.; Hu, H.; Hunter, D.; Janata, G.; Kupka, R.; Lanphear, B.; Lichtveld, M.; Martin, K.; Mustapha, A.; Sanchez-Triana, E.; Sandilya, K.; Schaefli, L.; Shaw, J.; Seddon, J.; Suk, W.; Téllez-Rojo, M. M.; Yan, C. Pollution and health: a progress update. *Lancet Planet. Health* **2022**, *6* (6), e535−e547.

(5) Zhou, P.; Li, X.; Zhou, J.; Peng, Z.; Shen, L.; Li, W. Insights of the adsorption mechanism of methylene blue on biochar from phytoextraction residues of Citrus aurantium L.: Adsorption model and DFT calculations. *J. Environ. Chem. Eng.* **2023**, *11* (5), No. 110496.

(6) Saeed, T.; Naeem, A.; Din, I. U.; Farooq, M.; Khan, I. W.; Hamayun, M.; Malik, T. Synthesis of chitosan composite of metal-organic framework for the adsorption of dyes; kinetic and thermodynamic approach. *J. Hazard. Mater.* **2022**, *427*, No. 127902.

(7) Obayomi, K. S.; Lau, S. Y.; Ibrahim, O.; Zhang, J.; Meunier, L.; Aniobi, M. M.; Atunwa, B. T.; Pramanik, B. K.; Rahman, M. M. Removal of Congo red dye from aqueous environment by zinc terephthalate metal organic framework decorated on silver nano-particles-loaded biochar: Mechanistic insights of adsorption. *Microporous Mesoporous Mater.* **2023**, *355*, No. 112568.

(8) Zourou, A.; Ntziouni, A.; Adamopoulos, N. D.; Roman, T.; Zhang, F.; Terrones, M.; Kordatos, K. V. Graphene oxide−MnFe2O4 nanohybrid material as an adsorbent of Congo red dye. *J. Phys. Chem. Solids* **2023**, *181*, No. 111490.

(9) Holkar, C. R.; Jadhav, A. J.; Pinjari, D. V.; Mahamuni, N. M.; Pandit, A. B. A critical review on textile wastewater treatments: Possible approaches. *J. Environ. Manage.* **2016**, *182*, 351−366.

(10) Agarwala, R.; Mulky, L. Adsorption of Dyes from Wastewater: A Comprehensive Review. *ChemBioEng Rev.* **2023**, *10* (3), 326−335.

(11) Rego, R. M.; Kurkuri, M. D.; Kigga, M. A comprehensive review on water remediation using UiO-66 MOFs and their derivatives. *Chemosphere* **2022**, *302*, No. 134845.

(12) Kouda, I.; Seddik, N. B.; Laaziz, A.; Hadri, M.; Draoui, K.; Elmidaoui, A. Efficient removal of cationic dye from wastewater using novel low-cost adsorbent, cellulose-clay composite: Insights from isotherm, kinetic, thermodynamic, and molecular dynamics simulation studies. *J. Mol. Struct.* **2023**, *1291*, No. 135865.

(13) Hamad, M. T. M. H. Optimization study of the adsorption of malachite green removal by MgO nano-composite, nano-bentonite and fungal immobilization on active carbon using response surface

https://doi.org/10.1021/acsomega.4c05680
ACS Omega 2024, 9, 41676−41686

methodology and kinetic study. *Environ. Sci. Eur.* **2023**, *35* (1), No. 26.
(14) Chinthala, M.; Balakrishnan, A.; Venkataraman, P.; Gowtham, V. M.; Polagani, R. K. Synthesis and applications of nano-MgO and composites for medicine, energy, and environmental remediation: a review. *Environ. Chem. Lett.* **2021**, *19* (6), 4415−4454.
(15) Smith, L. R.; Smith, P. J.; Mugford, K. S.; Douthwaite, M.; Dummer, N. F.; Willock, D. J.; Howard, M.; Knight, D. W.; Taylor, S. H.; Hutchings, G. J. New insights for the valorisation of glycerol over MgO catalysts in the gas-phase. *Catal. Sci. Technol.* **2019**, *9* (6), 1464−1475.
(16) Ahmad, K.; Mobin, S. M. Shape controlled synthesis of high surface area MgO microstructures for highly efficient congo red dye removal and peroxide sensor. *J. Environ. Chem. Eng.* **2019**, *7* (5), No. 103347.
(17) Perera, H. C. S.; Gurunanthanan, V.; Singh, A.; Mantilaka, M. M. M. G. P. G.; Das, G.; Arya, S. Magnesium oxide (MgO) nanoadsorbents in wastewater treatment: A comprehensive review. *J. Magnesium Alloys* **2024**, *12* (5), 1709−1773.
(18) Jangid, N. K.; Kaliraman, S.; Singh, A.; Srivastava, A.; Srivastava, M.; Jadoun, S.; Dwivedi, J.; Kaur, N. Removal of fluoride ions from water using MgO-based materials with special emphasis on MgO/PPy nanocomposites: A review. *J. Mol. Liq.* **2024**, *399*, No. 124473.
(19) Khan, A.; Naeem, A.; Mahmood, T.; Ahmad, B.; Ahmad, Z.; Farooq, M.; Saeed, T. Mechanistic study on methyl orange and congo red adsorption onto polyvinyl pyrrolidone modified magnesium oxide. *Int. J. Environ. Sci. Technol.* **2022**, *19* (4), 2515−2528.
(20) Li, J.; Zhang, Z.; Li, Y.; Gao, R.; Feng, R.; Pan, L.; Liu, G.; Ma, C.; Zhu, L. Citric acid steam-assisted decomposition method for the synthesis of meso-macroporous magnesium oxide with rich oxygen defects: Efficient removal and convenient recovery property of Congo red and Ni(II). *Ceram. Int.* **2024**, *50* (18), 31884−31895.
(21) Xu, J.; Xu, D.; Zhu, B.; Cheng, B.; Jiang, C. Adsorptive removal of an anionic dye Congo red by flower-like hierarchical magnesium oxide (MgO)-graphene oxide composite microspheres. *Appl. Surf. Sci.* **2018**, *435*, 1136−1142.
(22) Li, N.; Dang, H.; Chang, Z.; Zhao, X.; Zhang, M.; Li, W.; Zhou, H.; Sun, C. Synthesis of uniformly distributed magnesium oxide micro-/nanostructured materials with deep eutectic solvent for dye adsorption. *J. Alloys Compd.* **2019**, *808*, No. 151571.
(23) Zhang, Z.; Zhang, D.; Yue, C.; Liu, Z.; Mu, Y.; Yang, Z.; Dastan, D.; Zhang, X.; Yin, X.-T.; Ma, X. High sensitivity and surface mechanism of MOFs-derived metal oxide Co3O4-SnO2 hollow spheres to ethanol. *J. Alloys Compd.* **2023**, *962*, No. 171182.
(24) He, Z.; Wang, K.; Zhu, S.; Huang, L. A.; Chen, M.; Guo, J.; Pei, S.; Shao, H.; Wang, J. MOF-Derived Hierarchical MnO-Doped Fe(3)O(4)@C Composite Nanospheres with Enhanced Lithium Storage. *ACS Appl. Mater. Interfaces* **2018**, *10* (13), 10974−10985.
(25) Ouyang, Y. S.; Yang, Q. Y. High-Performance Visible-Light Photocatalysts for H(2) Production: Rod-Shaped Co(3)O(4)/CoO/Co(2)P Heterojunction Derived from Co-MOF-74. *J. Colloid Interface Sci.* **2023**, *644*, 346−357.
(26) Yuan, N.; Zhao, A.; Fang, K.; Wang, D.; Zhang, X. Diverse effects of metal−organic frameworks on microstructure and compressive strength of cement-based composites. *Cem. Concr. Compos.* **2022**, *127*, No. 104406.
(27) Hu, N.; Yu, J.; Hou, L.; Shi, C.; Li, K.; Hang, F.; Xie, C. Amine-functionalized MOF-derived carbon materials for efficient removal of Congo red dye from aqueous solutions: simulation and adsorption studies. *RSC Adv.* **2022**, *13* (1), 1−13.
(28) Wang, X.; Cheng, B.; Zhang, L.; Yu, J.; Li, Y. Synthesis of MgNiCo LDH hollow structure derived from ZIF-67 as superb adsorbent for Congo red. *J. Colloid Interface Sci.* **2022**, *612*, 598−607.
(29) Jiang, G.; Osman, S.; Senthil, R. A.; Sun, Y.; Tan, X.; Pan, J. Hierarchically porous carbon derived from magnesium-based metal-organic frameworks as advanced active material for supercapacitor. *J. Energy Storage* **2022**, *49*, No. 104071.
(30) Hosseini, M.; Ghanbari, M.; Dawi, E. A.; Mahdi, M. A.; Ganduh, S. H.; Jasim, L. S.; Ibrahim, A. M. M.; Salavati-Niasari, M. Investigations of nickel silicate for degradation of water-soluble organic pollutants. *Int. J. Hydrogen Energy* **2024**, *61*, 307−315.
(31) Li, S.; Hao, J.; Yang, S.; Wang, Y.; Li, Y.; E, T. Alginate-based adsorbents with adjustable slit-shaped pore structure for selective removal of copper ions. *Int. J. Biol. Macromol.* **2024**, *267*, No. 131484.
(32) Tran, B. L.; Chin, H.-Y.; Chang, B. K.; Chiang, A. S. T. Dye adsorption in ZIF-8: The importance of external surface area. *Microporous Mesoporous Mater.* **2019**, *277*, 149−153.
(33) Niu, C.; Zhang, N.; Hu, C.; Zhang, C.; Zhang, H.; Xing, Y. Preparation of a novel citric acid-crosslinked Zn-MOF/chitosan composite and application in adsorption of chromium(VI) and methyl orange from aqueous solution. *Carbohydr. Polym.* **2021**, *258*, No. 117644.
(34) Adli, N. M.; Shan, W.; Hwang, S.; Samarakoon, W.; Karakalos, S.; Li, Y.; Cullen, D. A.; Su, D.; Feng, Z.; Wang, G.; Wu, G. Engineering Atomically Dispersed FeN(4) Active Sites for CO(2) Electroreduction. *Angew. Chem., Int. Ed.* **2021**, *60* (2), 1022−1032.
(35) Dong, M.; Li, W.; Geng, L.; Ma, X.; Li, Y.; Fan, Y.; Khan, A. Defect-decorated Cu2MoS4 as a new efficient hydrogen evolution cocatalyst: Rich active sites, rapid charge transfer and optimized hydrogen adsorption. *Fuel* **2024**, *367*, No. 131484.
(36) Ediati, R.; Aulia, W.; Nikmatin, B. A.; Hidayat, A. R. P.; Fitriana, U. M.; Muarifah, C.; Sulistiono, D. O.; Martak, F.; Prasetyoko, D. Chitosan/UiO-66 composites as high-performance adsorbents for the removal of methyl orange in aqueous solution. *Mater. Today Chem.* **2021**, *21*, No. 100533.
(37) Chanthavong, V.; Prabhakar, M. N.; Lee, D. W.; Song, J.-i. Extraction of Cellulose Microfibers From Waste Fallen Dried Leaves and Fabrication of a Degradable Composite Film for Packaging Applications. *J. Inorg. Organomet. Polym. Mater.* **2024**, *34* (4), 1861−1875.
(38) Villarroel-Rocha, D.; Bernini, M. C.; Arroyo-Gómez, J. J.; Villarroel-Rocha, J.; Sapag, K. Synthesis of MOF-5 using terephthalic acid as a ligand obtained from polyethylene terephthalate (PET) waste and its test in CO2 adsorption. *Braz. J. Chem. Eng.* **2022**, *39* (4), 949−959.
(39) He, X.; Ma, C.; Wang, Z.; Zhang, M. Construction of Shape-Controlled MgO Microstructures by Natural Bischofite for Cost-Efficient Dye Adsorption. *ChemistrySelect* **2023**, *8* (1), No. e202203701.
(40) Yurtsever, H. A.; Çetin, A. E. Fabrication of ZIF-8 decorated copper doped TiO2 nanocomposite at low ZIF-8 loading for solar energy applications. *Colloids Surf., A* **2021**, *625*, No. 126980.
(41) Zhang, Y.-N.; Pei, Z.; Wang, Z.-H.; Wang, C.-E.; Liang, F.-F.; Wei, L.-Q. ZIF-8 modified by isocyanate as a photocatalytic antibacterial agent. *Rare Met.* **2024**, *43* (6), 2708−2718.
(42) Song, T.; Gao, F.; Du, X.; Hao, X.; Liu, Z. Removal of boron in aqueous solution by magnesium oxide with the hydration process. *Colloids Surf., A* **2023**, *665*, No. 131211.
(43) Cao, N.; Zhao, X.; Gao, M.; Li, Z.; Ding, X.; Li, C.; Liu, K.; Du, X.; Li, W.; Feng, J.; Ren, Y.; Wei, T. Superior selective adsorption of MgO with abundant oxygen vacancies to removal and recycle reactive dyes. *Sep. Purif. Technol.* **2021**, *275*, No. 119236.
(44) Zhao, S.; Wen, Y.; Liu, X.; Pen, X.; Lü, F.; Gao, F.; Xie, X.; Du, C.; Yi, H.; Kang, D.; Tang, X. Formation of active oxygen species on single-atom Pt catalyst and promoted catalytic oxidation of toluene. *Nano Res.* **2020**, *13* (6), 1544−1551.
(45) Liu, X.; Fu, J.; Tang, Y.; Smith, R. L., Jr; Qi, X. Mg-coordinated self-assembly of MgO-doped ordered mesoporous carbons for selective recovery of phosphorus from aqueous solutions. *Chem. Eng. J.* **2021**, *406*, No. 126748.
(46) Liu, Q.; Su, Q.; Cheng, W.; Ding, J.; Zhang, W.; Wang, J.; Wang, Y.; Wang, X.; Huang, Y. Dual role of Fe boost lattice oxygen oxidation of Mo-based materials from kinetics and thermodynamics. *Appl. Catal, B* **2024**, *340*, No. 123188.
(47) Zhu, Y.; Zhang, Z.; Li, W.; Lei, Z.; Cheng, N.; Tan, Y.; Mu, S.; Sun, X. Highly Exposed Active Sites of Defect-Enriched Derived

https://doi.org/10.1021/acsomega.4c05680
ACS Omega 2024, 9, 41676−41686

MOFs for Enhanced Oxygen Reduction Reaction. *ACS Sustainable Chem. Eng.* **2019**, *7* (21), 17855−17862.
(48) Wang, R.-D.; Wei, W.-M.; Li, H.; Shen, T.-Z.; Wang, L.; Zhou, S.-H.; Zhang, W.-Q.; Du, L.; Zhao, Q.-H. Metal-Organic framework derived vulcanized functional materials for ultra-efficient treatment of Hg(II) ions in water. *J. Mol. Liq.* **2024**, *401*, No. 124609.
(49) Zhang, X.; Wang, C.; Luan, C.; Liao, M.; Xu, W. Preparation of MOF-derived molybdenum-carbide-modified PtCu nano-alloy catalysts and their methanol oxidation performance. *New J. Chem.* **2024**, *48* (17), 7964−7971.
(50) Ye, J.; Jin, L.; Zhao, X.; Qian, X.; Dong, M. Superior adsorption performance of metal-organic-frameworks derived magnetic cobalt-embedded carbon microrods for triphenylmethane dyes. *J. Colloid Interface Sci.* **2019**, *536*, 483−492.
(51) Si, Y.; Li, J.; Cui, B.; Tang, D.; Yang, L.; Murugadoss, V.; Maganti, S.; Huang, M.; Guo, Z. Janus phenol−formaldehyde resin and periodic mesoporous organic silica nanoadsorbent for the removal of heavy metal ions and organic dyes from polluted water. *Adv. Compos. Hybrid Mater.* **2022**, *5* (2), 1180−1195.
(52) Dragan, E. S.; Humelnicu, D.; Dinu, M. V. Design of porous strong base anion exchangers bearing N,N-dialkyl 2-hydroxyethyl ammonium groups with enhanced retention of Cr(VI) ions from aqueous solution. *React. Funct. Polym.* **2018**, *124*, 55−63.
(53) Lu, N.; Hu, T.; Zhai, Y.; Qin, H.; Aliyeva, J.; Zhang, H. Fungal cell with artificial metal container for heavy metals biosorption: Equilibrium, kinetics study and mechanisms analysis. *Environ. Res.* **2020**, *182*, No. 109061.
(54) He, Y.; Li, Z.; Xue, M.; Qi, X.; Li, J.; Jiang, K.; Fu, J.; Guan, C.; Sun, K.; Shi, Z.; Sonoda, A.; Chu, H.; Wei, H. Enhanced adsorption performance of subordinate magnesium sites in pinhole magnesium oxide nanosheets with rich oxygen vacancies. *Environ. Funct. Mater.* **2022**, *1* (1), 105−113.
(55) Yap, P. L.; Nguyen, H. H.; Ma, J.; Gunawardana, M.; Losic, D. Exploring kinetic and thermodynamic insights of graphene related two dimensional materials for carbon dioxide adsorption. *Sep. Purif. Technol.* **2024**, *348*, No. 127633.
(56) Jain, M.; Garg, V. K.; Kadirvelu, K. Adsorption of hexavalent chromium from aqueous medium onto carbonaceous adsorbents prepared from waste biomass. *J. Environ. Manage.* **2010**, *91* (4), 949−957.
(57) Toptaş, Y.; Yavuz, B.; Korkmaz, A. A.; Önal, Y. Sustainable approach to dye adsorption: hemp-based activated carbon as an effective adsorbent. *Int. J. Environ. Anal. Chem.* **2024**, 1−26.
(58) Song, G.; Li, A.; Shi, Y.; Li, W.; Wang, H.; Wang, C.; Li, R.; Ding, G. Sorptive removal of methylene blue from water by magnetic multi-walled carbon nanotube composites. *Environ. Sci. Pollut. Res.* **2021**, *28* (30), 41268−41282.
(59) Gao, X.; Pan, H.; Qiao, C.; Liu, Y.; Zhou, C.; Zhai, Q.; Hu, M.; Li, S.; Jiang, Y. Facile preparation of MOF-derived MHCo3O4&Co/C with a hierarchical porous structure for entrapping enzymes: having both high stability and catalytic activity. *Catal. Sci. Technol.* **2022**, *12* (1), 84−93.
(60) Wang, R.; Liu, Y.; Lu, Y.; Liang, S.; Zhang, Y.; Zhang, J.; Shi, R.; Yin, W. Fabrication of a corn stalk derived cellulose-based bio-adsorbent to remove Congo red from wastewater: Investigation on its ultra-high adsorption performance and mechanism. *Int. J. Biol. Macromol.* **2023**, *241*, No. 124545.
(61) Cui, G.-Y.; Zhang, W.; Yang, J.-M. Selective adsorptive removal of anionic dyes from aqueous solutions using MIL-101@GO: Effect of GO. *Colloids Surf., A* **2023**, *667*, No. 131364.
(62) Liu, W.; Fan, C.; Zong, Z.; Li, N.; Ma, K.; Zhu, B.; Zhang, X.; Fan, Y. Two Co(II)-based metal organic frameworks for highly efficient removal of azo dyes from aqueous environment: Synthesis, selective adsorption and adsorption mechanism. *Colloids Surf., A* **2020**, *603*, No. 125236.
(63) Alhajeri, N. S.; Tawfik, A. Integrating biochar and microbial community for detoxification of wastewater industry containing analgesics. *J. Water Process Eng.* **2024**, *58*, No. 104767.
(64) Cao, M.; Liu, X.; Wang, W.; Gao, M.; Li, Y.; Yang, H. Functionalized Zn/Al N-doped carbon nanocomposites with tunable morphology: Synergistic ultrafast low-temperature synthesis and tetracycline adsorption. *Sep. Purif. Technol.* **2021**, *278*, No. 119548.
(65) Han, S.; Xie, H.; Zhang, L.; Wang, X.; Zhong, Y.; Shen, Y.; Wang, H.; Hao, C. High-performance polyethylenimine-functionalized lignin/silica porous composite microsphere for the removal of hexavalent chromium, phosphate and Congo red from aqueous solutions. *Ind. Crops Prod.* **2023**, *194*, No. 116289.
(66) Mohamed, R. M.; Shawky, A.; Mkhalid, I. A. Facile synthesis of MgO and Ni-MgO nanostructures with enhanced adsorption of methyl blue dye. *J. Phys. Chem. Solids* **2017**, *101*, 50−57.

https://doi.org/10.1021/acsomega.4c05680
ACS Omega 2024, 9, 41676−41686